Detached direct numerical simulations of turbulent two-phase bubbly channel flow

Igor A. Bolotnov *, Kenneth E. Jansen, Donald A. Drew, Assad A. Oberai, Richard T. Lahey Jr., Michael Z. Podowski

Center for Multiphase Research, Rensselaer Polytechnic Institute, 110 8th St., Troy, NY 12180, USA

ARTICLE INFO

ABSTRACT

DNS simulations of two-phase turbulent bubbly channel flow at Re_τ = 180 (Reynolds number based on friction velocity and channel half-width) were performed using a stabilized finite element method (FEM) and a level set approach to track the air/water interfaces.

Fully developed turbulent single-phase solutions obtained previously using the same stabilized FEM code were used as the initial flow field, and an appropriate level-set distance field was introduced to represent the air bubbles. Surface tension and gravity forces were used in the simulations to physically represent the behavior of a bubbly air/water two-phase flow having a liquid/gas density ratio of 858.3.

The simulation results were averaged to obtain the liquid and gas mean velocity distributions, the local void fractions as well as the local turbulent kinetic energy and dissipation rate of the liquid phase. The liquid phase parameters were compared with the corresponding single-phase turbulent channel flow to determine the bubbles' influence on the turbulence field.

© 2011 Elsevier Ltd. All rights reserved.

1. Introduction

The understanding of turbulent two-phase bubbly flows is important due to the widespread occurrence of this phenomenon in natural and engineering systems.

The turbulent bubbly flows in conduits have been extensively studied in the past using experimental techniques (Serizawa et al., 1975a,b; Wang et al., 1987). In particular, the gas volume fraction distribution, liquid mean velocity profiles and various properties of turbulence (e.g. turbulent kinetic energy) were measured and analyzed. It was observed that the size of the bubbles and their concentration affect void fraction profiles, including such characteristics as wall-peaking, coring and saddling (Serizawa et al., 1975a,b). Similar profiles were obtained in the presented multiphase DNS study.

Recent progress in the development of massively parallel computer systems and advanced numerical algorithms make the direct numerical simulation (DNS) of two-phase bubbly turbulent flows a viable approach to study this subject. Tryggvason et al. (2006) reviewed the current state of the DNS of dispersed bubbly gas/liquid flows. Earlier DNS applications to multiphase flows focused on rising bubbles in shear-free domains, including: homogeneous bubbly flows (Bunner and Tryggvason, 2003), laminar bubbly channel flows (Nagrath et al., 2005), and the decay of isotropic turbulence interactions with bubbles (Toutant et al., 2008). Other simulations of two-phase turbulent flows (Nierhaus et al., 2007) assumed negligibly small bubbles compared to the scales of turbulence (for the Reynolds number based on friction velocity, Re_τ = 131).

Lu and Tryggvason (2008) studied a turbulent bubbly upflow (Re_τ = 127) in a vertical channel using front-tracking/finite volume method. They observed that the void fraction profile is highly dependent on the deformability of the simulated bubbles. Pang et al. (2010) investigated a turbulent bubbly flow (Re_τ = 150) in microgravity conditions using DNS for the liquid and Lagrangian particle tracking approach for the bubbles.

In this manuscript we add to the growing database on the DNS of bubbly flows by simulating turbulent channel flows with bubbles of different sizes.

The two-phase turbulent bubbly channel flow simulations presented in this paper were performed using a stabilized finite element based approach and a level set method. The simulations included the effect of buoyancy, corresponding to a water/air density ratio of 858.3, and of the surface tension force. The liquid turbulence Reynolds number based on friction velocity (Re_τ) was about of 180. The level set method, which was used to track the air/water interfaces, allowed for possible coalescence and break-up of the bubbles.

The major novel aspects of the paper include the following:

- The current DNS simulations of gas/liquid two-phase flows correspond to Reynolds numbers 20–50% higher than those previously published (Nierhaus et al., 2007; Lu and Tryggvason, 2008; Pang et al., 2010), and they include the effect of bubble deformation and coalescence.

* Corresponding author. Present address: Nuclear Engineering Department at North Carolina State University, Campus Box 7909, Raleigh, NC 27695-7909, USA.
E-mail address: igor_bolotnov@ncsu.edu (I.A. Bolotnov).

- Detailed average characteristics of two-phase flow turbulence have been investigated, such as local distributions of turbulent kinetic energy and kinetic energy dissipation rate.
- The impact of bubble-induced turbulence on the "logarithmic law of the wall" has been analyzed for different gas concentrations and bubble sizes.
- Issues have been discussed where further progress in the modeling and computer simulation of two-phase flows is strongly coupled to the availability of new experimental data.

2. Numerical method

2.1. Governing equations

The spatial and temporal discretization of the Incompressible Navier–Stokes (INS) equations within the FEM code PHASTA has been described in Whiting (1999) and Nagrath (2004). The strong form of the INS equations is given by:

$$\text{Continuity}: \quad u_{i,j} = 0 \tag{1}$$
$$\text{Momentum}: \quad \rho u_{i,t} + \rho u_j u_{i,j} = -p_{,i} + \tau_{ij,j} + f_i \tag{2}$$

where ρ is density, u_i is ith component of velocity, p is the static pressure, τ_{ij} is the viscous stress tensor, and f_i represents the body force along the ith coordinate. For the incompressible flow of a Newtonian fluid, the viscous stress tensor is related to the fluid's viscosity, μ, and the strain rate tensor, S_{ij}, as:

$$\tau_{ij} = 2\mu S_{ij} = \mu(u_{i,j} + u_{j,i}) \tag{3}$$

Using the Continuum Surface Tension (CST) model of Brackbill et al. (1992), the surface tension force is computed as a local interfacial force density, which is included in f_i.

2.2. Level set method

The level set method of Sussman (Sussman et al., 1998, 1999; Sussman and Fatemi, 1999) and Sethian (1999) involves modeling the interface as the zero-level set of a smooth function, φ, where φ is often called the first scalar and it represents the signed distance from the interface. Hence, the interface is defined by $\varphi = 0$. The scalar, φ, is convected within a moving fluid according to,

$$\frac{D\varphi}{Dt} = \frac{\partial\varphi}{\partial t} + \underline{u} \cdot \nabla\varphi = 0 \tag{4}$$

where $\underline{u}$ is the flow velocity vector. Phase-1, the liquid phase, is indicated by a positive level set, $\varphi > 0$, and phase-2, the gas, by a negative level set, $\varphi < 0$. Since evaluating the jump in physical properties using a step change across the interface leads to poor computational results, the properties near an interface were defined using a smoothed Heaviside kernel function, H_ε, given by (Sussman et al., 1999):

$$H_\varepsilon(\varphi) = \begin{cases} 0, & \varphi < -\varepsilon \\ \frac{1}{2}\left[1 + \frac{\varphi}{\varepsilon} + \frac{1}{\pi}\sin\left(\frac{\pi\varphi}{\varepsilon}\right)\right], & |\varphi| < \varepsilon \\ 1, & \varphi > \varepsilon \end{cases} \tag{5}$$

where ε is the interface half-thickness.

The fluid properties are then defined as:

$$\rho(\varphi) = \rho_1 H_\varepsilon(\varphi) + \rho_2(1 - H_\varepsilon(\varphi)) \tag{6}$$
$$\mu(\varphi) = \mu_1 H_\varepsilon(\varphi) + \mu_2(1 - H_\varepsilon(\varphi)) \tag{7}$$

Although the solution may be reasonably good in the immediate vicinity of the interface, the distance field may not be correct throughout the domain since the varying fluid velocities throughout the flow field distort the level set contours. Thus, the level set was corrected with a re-distancing operation by solving the following PDE (Sussman and Fatemi, 1999):

$$\frac{\partial d}{\partial \tau} = S(\varphi)[1 - |\nabla d|] \tag{8}$$

where d is a scalar that represents the corrected distance field and τ is the pseudo time over which the PDE is solved to steady-state. This may be alternately expressed as the following transport equation:

$$\frac{\partial d}{\partial \tau} + \underline{w} \cdot \nabla d = S(\varphi) \tag{9}$$

The so-called second scalar, d, is originally assigned the level set field, φ, and is convected with a pseudo velocity, $\underline{w}$, where,

$$\underline{w} = S(\varphi)\frac{\nabla d}{|\nabla d|} \tag{10}$$

and $S(\varphi)$ is defined as:

$$S(\varphi) = \begin{cases} -1, & \varphi < -\varepsilon \\ \left[\frac{\varphi}{\varepsilon} + \frac{1}{\pi}\sin\left(\frac{\pi\varphi}{\varepsilon}\right)\right], & |\varphi| < \varepsilon \\ 1, & \varphi > \varepsilon \end{cases} \tag{11}$$

Note that the zeroth level set, or interface, $\varphi = 0$, does not move since its convecting velocity, $\underline{w}$, is zero. Solving the second scalar to steady-state restores the distance field to $\nabla d = \pm 1$ but does not alter the location of the interface. The first scalar, φ, is then updated using the steady solution of the second scalar, d.

Sussman et al. (1999) and Sussman and Fatemi (1999) proposed an additional constraint to be applied during the re-distancing step to help ensure the interface ($\varphi = 0$) does not move. It has been found in the present work that imposing this constraint also improves the convergence of the re-distancing step. The essence of the constraint is to preserve the original volume (i.e., mass) of each phase during the re-distance step.

3. Discussion

3.1. Computational domain and grid

The goal of the two-phase bubbly flow simulation is to represent a number of adequately resolved bubbles in a turbulent channel flow domain. In order to have bubbles which were relatively small compared to the size of the channel the following domain parameters were used (refer to Fig. 1):

- stream wise (x) length: $L_x = 2\pi$;
- channel width (y): $L_y = 2.0$;
- span wise (z) length: $L_z = \frac{2}{3}\pi$.

This represents a quarter of the domain size previously used (Moser et al., 1999; Trofimova et al., 2009) in turbulent single-phase DNS: $L_x = 4\pi$, $L_y = 2.0$, $L_z = \frac{4}{3}\pi$.

The mesh resolution used in the present simulations was chosen to accurately represent the bubble/liquid interfaces by having at least 18 elements across the diameter of a typical spherical bubble. Also, the small bubble diameters were chosen to represent one eighth of the channel width. The mesh parameters are summarized in Table 1.

The computational mesh was isotropic with 9.8 M hexahedral elements. This mesh was used to perform the following simulations in the turbulent channel:

- Simulations with a single small bubble (case-1).
- Simulations with multiple (32) small bubbles (case-2).
- Simulations with a single large bubble (case-3).

In all cases, bubbles were superimposed onto a predetermined fully developed turbulent single phase channel flow field by supplying the solution with an analytical expression for the initial
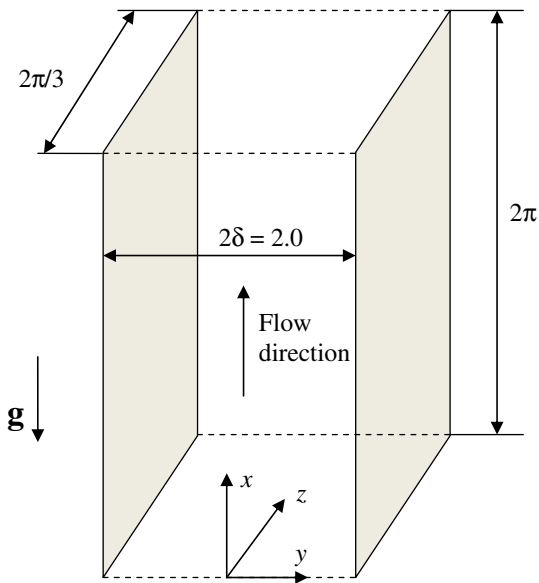
Fig. 1. Simulation domain dimensions and axis orientation. Walls are shown as shaded areas.

level set distance field representing the bubble(s). Table 2 summarizes the parameters of the three two-phase turbulent channel flow simulations presented herein.

3.2. Turbulent single-phase channel flow

A single-phase turbulent channel flow DNS solution obtained using the stabilized FEM code PHASTA-IC was used as a reference. Several single-phase DNS results based on PHASTA-IC have been published by Trofimova et al. (2009). In particular, comparisons against the data of Moser et al. (1999) included: mean velocity, RMS velocity fluctuations, shear stress, and a two-point correlation validation. However, due to restrictions imposed on the domain and the grid for the two-phase flow simulations with multiple bubbles, the single phase turbulence field had to be re-computed for this two-phase flow problem setup.

The current approach of achieving a statistically steady turbulent single-phase channel flow was considerably different from what has been used in other studies. Since we did not start with

Table 1
Hexahedral mesh parameters used for two-phase turbulent channel flow DNS.

Mesh parameters	Stream wise direction, x	Normal to the wall direction, y	Span wise direction, z
Resolution in wall units, Δx_i^+	2.5	2.5	2.5
Number of nodes	452	144	151

Table 2
Bubble size and volume fractions in the two-phase flow simulations.

Case number	1	2	3
Bubble diameter (in number of hexahedral elements)	18	18	72
Bubble diameter (in wall units)	45	45	180
Bubble diameter (in length units)	0.25	0.25	1.0
Number of bubbles	1	32	1
Volume of the bubbles	0.00818	0.2618	0.5236
Channel volume	26.319	26.319	26.319
Bubble volume fraction (i.e., global void fraction)	0.031%	1.0%	2.0%

a coarse mesh any attempt to invoke the turbulence using the Poiseuille flow (parabolic) with random perturbations resulted in flow re-laminarization. This can be explained by the fact that the random initial perturbations on a finer mesh excite small scales in the flow which are very strongly influenced by the molecular viscosity, compared to larger scales. Thus, in order to initialize the single-phase turbulent channel flow runs, we initially introduced a combination of a parabolic profile with cosine perturbation waves which have scales comparable with the channel width. This caused the flow to become turbulent and the problem was then run until a statistically stationary state was achieved. Note that the Reynolds number of the single-phase flow is 2734 based on the mean velocity and half-channel width (Eq. (18)). This makes the flow more stable compared to high Reynolds number turbulent channel flows.

Note that a laminar channel flow losses stability with respect to a small perturbation at a Reynolds number of about 3850 based on mean velocity and half-channel width (Orszag, 1971). Thus, additional effort is required to invoke turbulence at the Reynolds number under consideration in this study.

In order to resolve the bubbles everywhere in the channel we used a uniform mesh. This requirement lead to a large mesh and the first point off the wall at $y_1^+ = 2.5$. This resolution at the wall was insufficient to resolve the laminar sublayer and hence to impose the no-slip boundary condition. Thus we resorted to a friction-type of boundary condition that is described below (Nicoud et al., 1998):

- for each node on the wall, the corresponding node closest in the wall-normal direction is determined,
- the distance from the wall (y) and the average velocity parallel to the wall ($u_{\parallel}$) is recorded at this node,
- based on this information the nonlinear equation below, which is an expression for the Law of the Wall due to Spalding (1961), is solved iteratively to determine local friction velocity (u_τ):

$$y^+ = u^+ + \frac{1}{E}\left[\exp(\kappa_0 u^+) - 1 - (\kappa_0 u^+) - \frac{(\kappa_0 u^+)^2}{2!} - \frac{(\kappa_0 u^+)^3}{3!}\right] \quad (12)$$

where $y^+ = \frac{u_\tau y}{\nu}$ is the non-dimensional distance from the wall, $u^+ = \frac{u_{\parallel}}{u_\tau}$ is the parallel to the wall non-dimensional averaged velocity, κ_0 and C are von Karman constants ($E = \exp(C)$).

- the wall shear stress is determined form the friction velocity $\left(\tau_w = \rho_l u_\tau^2\right)$ and directly applied to the wall-node under consideration.

This procedure yields satisfactory results permitting the complex simulations become more affordable. Fig. 2 compares the near wall velocity profiles obtained using the described approach with another single-phase DNS simulation where the wall was resolved $\left(\Delta y_1^+ = 1.0\right)$ and "no-slip" velocity boundary condition was applied. We also provide the Law of the Wall plots in the laminar sublayer $(u^+ = y^+)$ and the in the logarithmic region $(u^+ = \frac{1}{\kappa_0} \ln y^+ + C, \kappa_0 = 0.39$ and $C = 5.5)$.

To further validate the application of the slip-velocity boundary condition for the simulation of the turbulent flows the Reynolds stress components have been compared with the results of Moser et al. (1999). The normal stresses are represented with the root mean square (RMS) velocity fluctuations and show the consistent agreement (Fig. 3).

Fig. 4 demonstrates that the shear stress distribution obtained using the slip-velocity boundary condition is also fully consistent with the same result published by Moser et al. (1999).

Fig. 1 shows the dimensions of the computational domain used in the presented simulations. Note that the flow occurs in the positive direction of x axis and the gravity force acts against the flow.
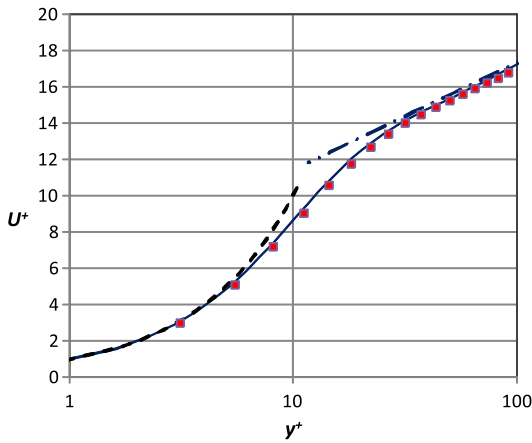
Fig. 2. Average liquid velocity profiles obtained using refined DNS at the wall (solid line), slip-velocity boundary condition approach (symbols) compared with the law of the wall (dashed and dash-dotted lines).
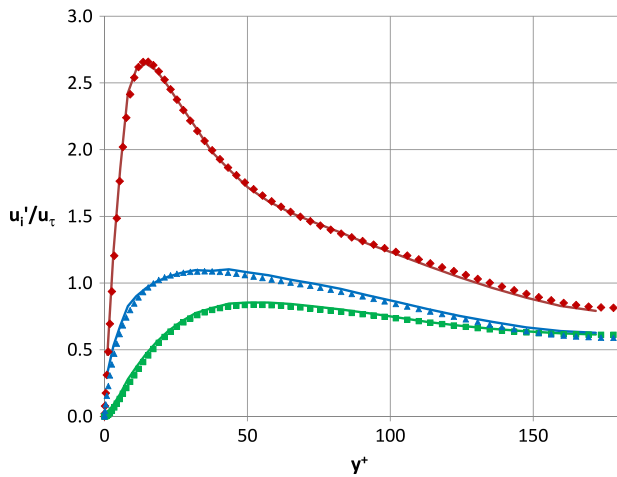

Fig. 3. Normalized RMS (root mean square) velocity fluctuations obtained using slip-velocity boundary conditions in the presented single-phase simulations (solid lines) compared to the results of Moser et al. (1999) (symbols) for the $Re_\tau = 180$ (stream-wise component shown in red; wall-normal in green and span-wise in blue). (For interpretation of the references to colour in this figure legend, the reader is referred to the web version of this article.)
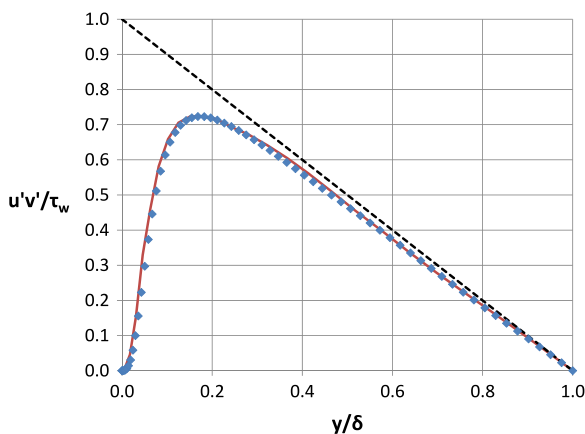

Fig. 4. Normalized turbulent shear stress distribution obtained using the slip-velocity boundary condition (solid line) compared to the results of Moser et al. (1999) (symbols). A total stress distribution is shown with dashed line.

Fig. 5 shows a typical instantaneous velocity field in a single-phase turbulent channel flow which was used as the initial condition for two-phase flow DNS runs.

3.3. Two-phase bubbly turbulent channel flows

For all two-phase flows studied the following steps were taken to initialize the turbulent channel bubbly flow simulations:

- a level set distance field was introduced with an analytical expression representing the interface of spherical bubble(s) at prescribed location(s) and size,
- the turbulent flow simulation started initially with identical fluid properties (density, ρ, and molecular viscosity, μ) for both fluids,
- gas phase density and viscosity were then ramped down to the desired values over one flow through of the periodic computational domain.

Let consider these steps in details. The general form of the initial distance field, ϕ_0, for bubbly flow simulations is:

$$\varphi_0 = \min_{i=1,N_b} \left[\sqrt{(x-x_i)^2 + (y-y_i)^2 + (z-z_i)^2} \right] - R \tag{13}$$

where N_b is the number of bubbles in the simulation, (x_i, y_i, z_i) is the coordinates of the centers of the bubbles and R is the bubbles' radius. The initial bubble distributions for the three simulations are shown in Fig. 6.

All three simulations were for vertical flow between parallel plates. The liquid/gas relative velocity was introduced by applying a gravity body force downwards while having a pressure gradient acting to overcome the combined effects of gravity and wall friction forces. To ensure a smooth transition between the single and two-phase turbulent channel flow simulations, we have used a numerical ramp to slowly change the properties of the gas phase (phase-2):

$$\rho_2(t) = \begin{cases} \rho_l, & \text{if } t < t_0 \\ \rho_l(1-\xi) + \rho_g\xi, & \text{if } t_0 \leqslant t \leqslant t_1 \\ \rho_g, & \text{if } t > t_1 \end{cases} \tag{14}$$

$$\mu_2(t) = \begin{cases} \mu_l, & \text{if } t < t_0 \\ \mu_l(1-\xi) + \mu_g\xi, & \text{if } t_0 \leqslant t \leqslant t_1 \\ \mu_g, & \text{if } t > t_1 \end{cases} \tag{15}$$

where $\xi = \frac{t-t_0}{t_1-t_0}$ is the linear ramp parameter, t_0 is the time of the start of the ramp, t_1 is the end ramp time and t is the current
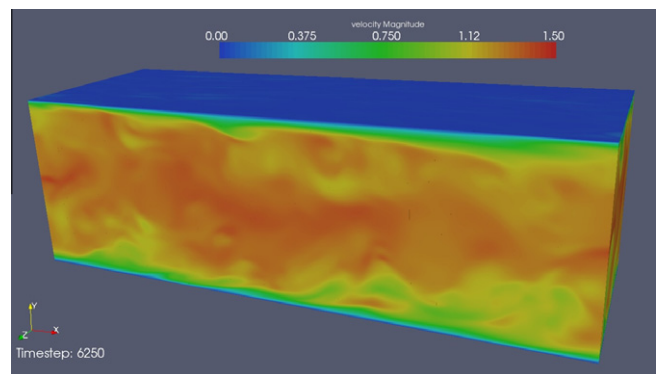

Fig. 5. Velocity magnitude in a single-phase turbulent channel flow solution used to initialize the two-phase simulations.
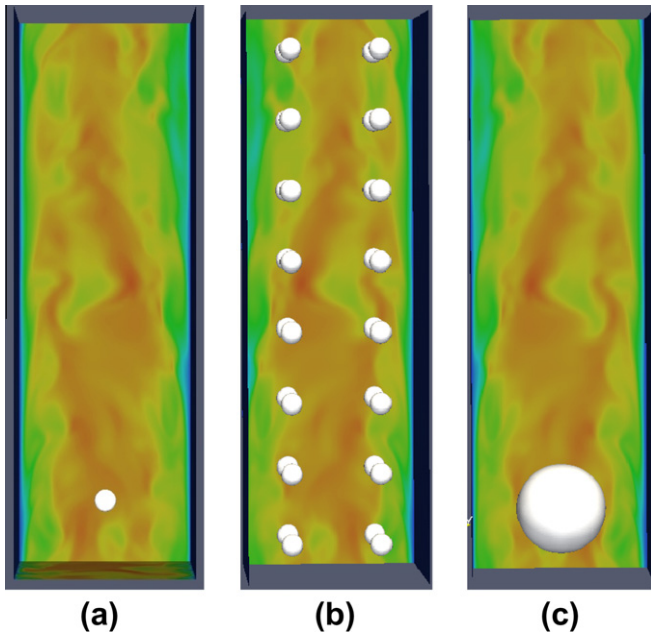
Fig. 6. Initial bubble distribution in the three cases of interests.

Fig. 7. Bubble/wall interaction and the repellant force application region.

simulation time. A typical ramp time, $t_1 - t_0$, was about one flow-through time for the periodic domain.

Since the interface tracking method we use does not incorporate any physical behavior of the gas/liquid/solid interactions (e.g., the repellant lubrication force between the wall and the near-wall bubbles, or the contact angle between the wall and interface) we initially experienced an effect of bubbles attaching to the channel walls. While this is possible for certain fluids at certain conditions, it is not expected for these air/water flows. Thus, in order to perform the simulations of the air/water flows of interest in this paper we introduced a subgrid bubble repellant lubrication like force which acts on the interface near the wall. The following expression was used for this subgrid repellant force (Clift et al., 1978):

$$\underline{F_r} = \mu_l U_l R \left(\frac{a_1}{d_w} + \frac{a_2}{d_w^2} \right) \underline{n_w} \qquad (16)$$

where U_l is the local mean axial liquid velocity, R is the bubble radius, d_w is the distance normal to the wall at the point of application, $\underline{n_w}$ is the normal to the wall, and $a_1 = 550.0$ and $a_2 = 35.0$ are model coefficients. This subgrid force was only applied on the liquid/gas interface ($|\phi| < \varepsilon_{ls}$) and close to the wall (i.e., $d_w < 4.0\varepsilon_{ls}$). The near-wall force application region is highlighted in blue on the right of the domain shown in Fig. 7.

This lubrication-type of force is only applied throughout the interface thickness (bounded by the pair of yellow lines parallel to the black zero level set contour). In this figure, the repellant force is directed to the left, normal to the wall. It has the effect of not letting the bubbles touch the wall, which is in agreement with experimental observations (Lance et al., 1996). The use of this subgrid force greatly simplifies the simulations, and, by analogy to single-phase *detached* eddy simulations (DES), we call this approach a *detached* direct numerical simulation (DDNS).

3.4. Dimensional interpretation of the two-phase simulations

The detached direct numerical simulations (DDNS) presented in this paper were performed using a non-dimensional set of parameters. While 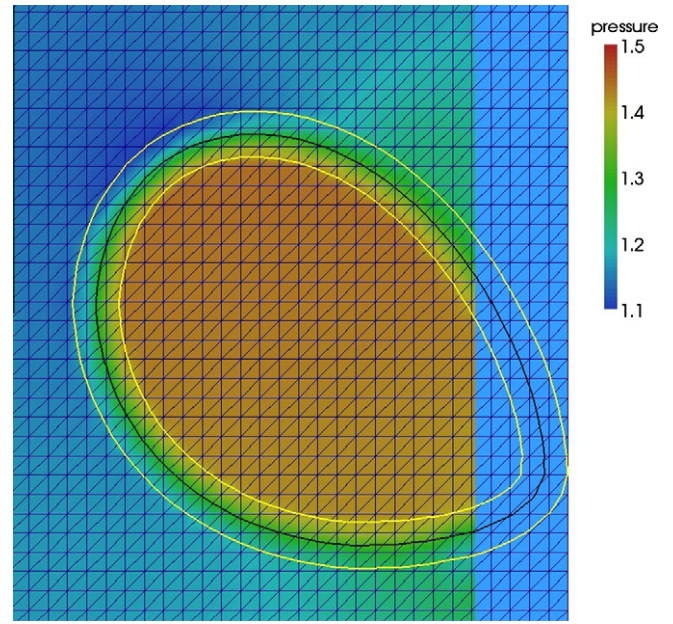for single-phase simulations the flow between parallel plates is well characterized by the Reynolds number, the complexity of a two-phase flow requires a more detailed description of the physical interpretation of the modeled flow. This section will discuss the size, surface tension, density and other parameters for the cases under consideration. For each parameter of interest, β, we will use the following notation:

- $\tilde{\beta}$ is the non-dimensional parameter used in the PHASTA simulations,
- β^* is a characteristic value of the parameter,
- $\beta = \beta^* \tilde{\beta}$ is the physically significant dimensional value of the parameter.

The single-phase simulations we have performed used the following non-dimensional parameters (density, dynamic viscosity, channel half-width, mean liquid velocity):

$$\tilde{\rho}_1 = 1.0, \quad \tilde{\mu}_1 = 0.00036574, \quad \tilde{\delta} = 1.0, \quad \widetilde{U}_m = 1.0 \qquad (17)$$

This set of parameters results in the following Reynolds number based on the half-channel width and mean liquid velocity:

$$\text{Re} = \frac{\tilde{\rho}\widetilde{U}\tilde{\delta}}{\tilde{\mu}} = 2734 \qquad (18)$$

The corresponding bulk Reynolds number based on the hydraulic diameter of the channel, $D_h = 4\tilde{\delta}$, was about 11,000, so that the conditions in the simulations corresponded to fully-developed turbulent flow. If we assume that the liquid is water at room temperature, the dimensional density and dynamic viscosity were:

$$\rho_1 = 996.5 \ \frac{\text{kg}}{\text{m}^3}, \quad \mu_1 = 0.0008541 \ \frac{\text{kg}}{\text{m s}} \qquad (19)$$

In this case the characteristic density and viscosity are defined as:

$$\rho^* = \frac{\rho_1}{\tilde{\rho}_1} = 996.5 \ \frac{\text{kg}}{\text{m}^3}, \quad \mu^* = \frac{\mu_1}{\tilde{\mu}_1} = 2.3279 \ \frac{\text{kg}}{\text{m s}} \qquad (20)$$

In order to determine the three basic scaling quantities (length, mass and time) we need one more parameter. Thus we chose the following characteristic length scale:

$$l^* = 3.6283 \times 10^{-3} \ \text{m} \qquad (21)$$

By performing a dimensional analysis of the specified characteristic quantities we can dimensionalize all the parameters of the problem. Table 3 summarizes the relations between various physical quantities for the small and large bubble simulation cases.

Given the chosen fluid properties and characteristic length the small bubble turbulent channel flow simulations can be interpreted as the flow of water at standard temperature and pressure (STP) between vertical parallel plates having a spacing of 7.25 mm. The periodic domain length was 22.8 mm, and the mean velocity of the liquid was 0.7114 m/s.

3.5. The results of numerical simulations

The numerical simulations were carried out over a time interval corresponding to several flow-throughs of the periodic domain by the liquid phase after the initial density and viscosity ramping was completed.

Figs. 8–10 show the motion of gas bubbles along the channel. The five snapshots shown in each figure are equally spaced in time (with time increasing to the right, see overview in Table 4). In each snapshot of the flow, the left and right boundaries are the walls, top and bottom boundaries have inflow/outflow periodicity condi-

tions and the velocity magnitude colors are shown for one plane normal to the viewer's direction. The bubbles interfaces are presented in three dimensions and do not necessarily intersect with the liquid flow field shown.

Fig. 8 shows the simulation representing a single small air bubble in the turbulent flow of water between parallel plates. The initial bubble diameter was 0.9 mm, corresponding to 1/8 of the distance between the plates. The motion of the bubble through the domain takes about 0.035 s. We can observe the bubble/wall interaction as it bounces off the wall and approaches it again later in the run. The time of these bubble/wall interactions is not uniform due to the influence of the turbulent liquid fluctuations on the bubble's trajectory. The approximate frequency of the wall/bubble interactions was about 0.2 in terms of the bulk timescale based frequency.

Fig. 9 shows a multiple bubble turbulent channel flow (i.e., 32 spherical bubbles initially). Each bubble has equivalent diameter of 0.9 mm (Table 5) and all the flow conditions are the same as in the single bubble case described for Fig. 8.

Since we have used a uniform mesh for all simulations in order to resolve the bubbles in any domain location, the computational cost for the 32 bubble simulation was essentially the same as for

Table 3
Reference values of characteristic parameters.

| Notation	Name	Relation	Small bubble cases	Large bubble case	Units
ρ^*	Density	Specified liquid/gas property	996.5	996.5	$\frac{kg}{m^3}$
μ^*	Dynamic viscosity	Specified liquid/gas property	2.3279	2.3279	$\frac{kg}{m\,s}$
l^*	Length	Specified channel half-width	0.0036283	0.005	m
m^*	Mass	$\rho^* l^{*3}$	4.76×10^{-5}	1.2456×10^{-4}	kg
t^*	Time	$\frac{\rho^* l^2}{\mu^*}$	5.635×10^{-3}	1.0702×10^{-2}	s
u^*	Velocity	$\frac{\mu^*}{\rho^* l^*}$	0.6438	0.4672	$\frac{m}{s}$
∇p^*	Pressure gradient	$\frac{\mu^{*2}}{\rho^* l^{*3}}$	1.1385×10^5	4.3505×10^4	$\frac{N}{m^3}$
g^*	Gravity acceleration	$\frac{\mu^{*2}}{\rho^{*2} l^{*3}}$	114.25	43.66	$\frac{m}{s^2}$
σ^*	Surface tension	$\frac{\mu^{*2}}{\rho^* l^*}$	1.5	1.0876	$\frac{N}{m}$
τ_w^*	Wall shear	$\frac{\mu^{*2}}{\rho^* l^{*2}}$	413.09	217.53	$\frac{N}{m^2}$
k^*	Turbulent kinetic energy	$\frac{\mu^{*2}}{\rho^{*2} l^{*2}}$	0.4145	0.2183	$\frac{m^2}{s^2}$
ε^*	Turbulent dissipation rate	$\frac{\mu^{*3}}{\rho^{*3} l^{*4}}$	73.56	20.40	$\frac{m^2}{s^3}$
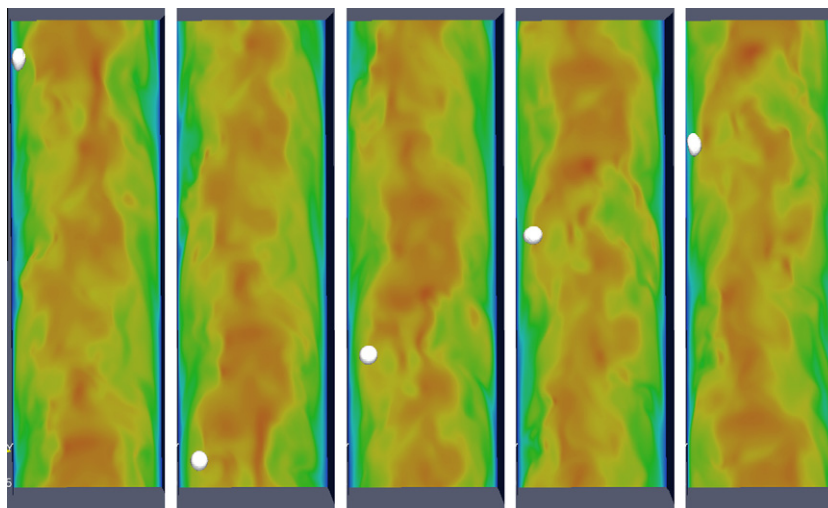
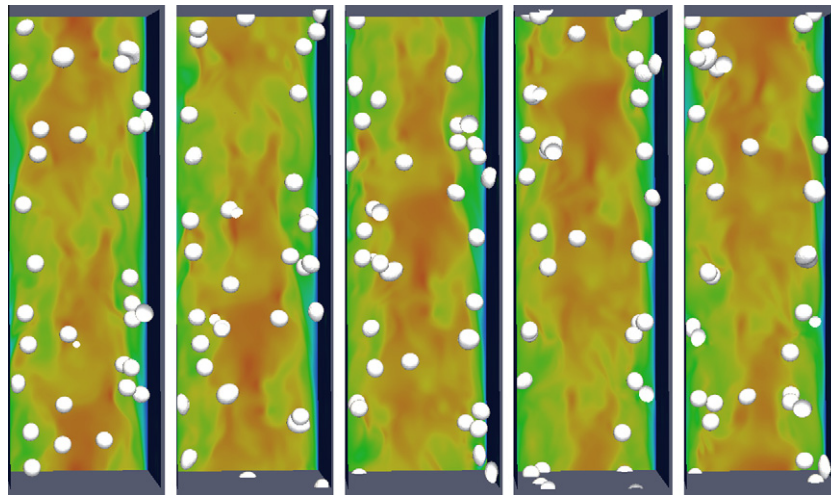**Fig. 8.** Single bubble turbulent channel flow evolution.

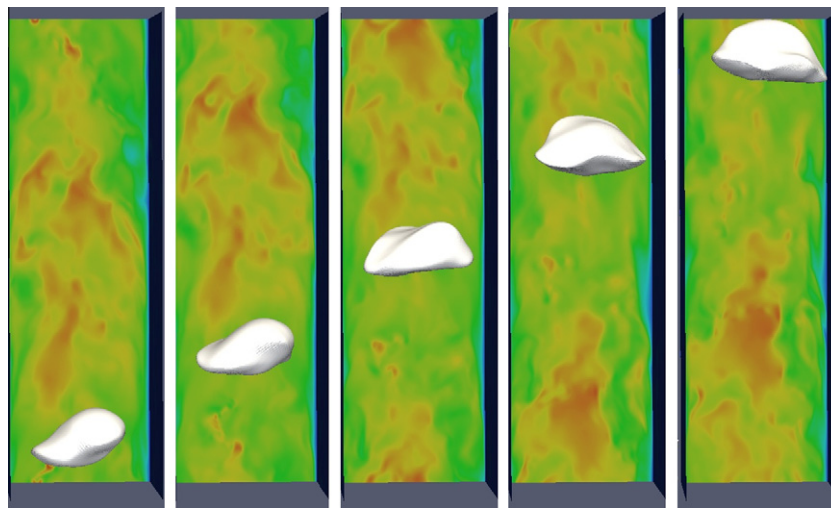**Fig. 9.** Multiple bubble turbulent channel flow simulation.

Fig. 10. Large bubble turbulent channel flow simulation.

Table 4
Overview of sampling times provided for flow visualization.

Case:	Single bubble	Multiple bubbles	Large bubble
Number of snapshots	5	5	5
Sampling interval, time steps	575	650	550
Sampling interval, bulk time units	1.13	1.097	0.74

a single bubble. Significantly, the affinity of the bubbles to concentrate near the walls is in agreement with experimental observations (Lance et al., 1996).

The third simulation presented in the paper deals with a single large bubble in the same domain. The equivalent bubble diameter was 5.0 mm which represents half of the channel width, δ (Table 5). However, once the flow becomes developed, the bubble takes a cap-like shape and actually stretches across about 75% of the distance between the parallel plates. Fig. 10 shows typical large bubble behavior during one flow through of the simulation. Table 5 summarizes the various dimensional parameters used in the present simulations for both multiple bubble and large bubble cases.

The values of the following non-dimensional numbers are also shown in Table 5:

- Eotvos number: $\text{Eo} = \frac{(\rho_l - \rho_g)gd^2}{\sigma}$.
- Morton number: $\text{Mo} = \frac{g\mu_l^4(\rho_l - \rho_g)}{\rho_l^2\sigma^3}$.
- Weber number: $\text{We} = \frac{\rho_l U^2 d}{\sigma}$.

3.6. Computational cost

The two-phase detached direct numerical simulation of turbulent channel flow was carried out for about 7 flow-through cycles in the periodic domain in each case in order to obtain statistically-stationary solutions. One flow-through cycle took approximately 3000 time steps. PHASTA was run in parallel on 2048 processors (which represents a computational speed of approximately 4.4 teraflop) using a BlueGene/L super computer at the Computational Center for Nanotechnology Innovation (CCNI) of Rensselaer Polytechnic Institute (RPI).

Two 12 h runs were required to go through 3000 time steps and complete one flow-through cycle for each case. Thus, approximately 50,000 CPU-hours on a BlueGene/L massively parallel supercomputer was used for each flow-through cycle. Therefore,

Table 5
Overview of non-dimensional and dimensional quantities for multiple bubble and large bubble simulations.

Quantity of interest	Multiple bubble case: non-dimensional value	Multiple bubble case: dimensional value	Large bubble case: non-dimensional value	Large bubble case: dimensional value
Channel width, 2δ	2.0	7.2566 mm	2.0	10.0 mm
Bubble diameter	0.25	0.9 mm	1.0	5.0 mm
Liquid superficial velocity	1.1050	0.7114 m/s	1.1756	0.5492 m/s
Liquid density	1.0	996.5 kg/m^3	1.0	996.5 kg/m^3
Liquid dynamic viscosity	0.00036574	0.0008514 kg/m s	0.00036574	0.0008514 kg/m s
Reynolds number based on hydraulic diameter	12,085	12,085	12,857	12,857
Gravity, g	0.08578	9.8 m/s^2	0.22448	9.8 m/s^2
Imposed pressure gradient, ∇p	0.09002	10.2488 kPa/m	0.22872	9.950 kPa/m
Surface tension, σ	0.0487	0.073 kg/s^2	0.03356	0.0365 kg/s^2
Global void fraction, $\langle \alpha \rangle$	0.0117	0.0117	0.02	0.02
Mixture density, ρ_m	0.98831363	984.85 kg/m^3	0.9800233	976.59 kg/m^3
Gravitational force, $\rho_m g$	0.08478	9.652 kN/m^3	0.2200	9.571 kN/m^3
Wall shear	0.00524246	2.1656 N/m^2	0.0087244	1.8978 N/m^2
Eotvos number		0.110		6.689
Morton number		1.33×10^{-11}		1.06×10^{-10}
Weber number		6.268		41.181

to produce the final results run required about 350,000 CPU-hours for each case presented. To perform ensemble averaging (discussed below) we performed and averaged five separate simulations of the 32 bubble case to improve the statistical results. Thus, the overall computational cost for the results presented in this paper was about 2.45 million CPU-hours.

4. Two-phase turbulence statistics

For each case presented herein time and space averaging has been performed to compute basic two-phase turbulent flow parameters, such as the local mean velocity (U_i) for each phase, the gas volume (i.e., void) fraction distribution (α), the turbulent kinetic energy (k) and the turbulence dissipation rate distribution of the liquid phase (ε).

We performed a sliding window time average to make sure that a statistically stationary solution was obtained after the initial start-up transient. To obtain better statistics we also employed an ensemble averaging technique by performing several DNS runs of the same problem with slightly different initial conditions and averaged the results among them. The analysis results in the local, time-dependent functions of the following parameters:

$$\text{Mean velocity}: U_i^k(t) = \frac{1}{\alpha_k N_e} \sum_{m=1}^{N_e} \left(\frac{1}{N_w} \sum_{j=1}^{N_w} X_k u_m^i(t+t_j) \right) \quad (22)$$

Turbulent kinetic energy :

$$k^k(t) = \frac{1}{\alpha_k N_e} \sum_{m=1}^{N_e} \left(\frac{1}{N_w} \sum_{j=1}^{N_w} X_k \times \sum_{i=1}^{3} \frac{1}{2} \left(u_m'^i(t+t_j) \right)^2 \right) \quad (23)$$

Turbulent dissipation rate :

$$\varepsilon^k(t) = v \frac{1}{\alpha_k N_e} \sum_{m=1}^{N_e} \left(\frac{1}{N_w} \sum_{j=1}^{N_w} \sum_{i=1}^{3} \sum_{k=1}^{3} X_k \times \left(\frac{\partial u_m'^i(t+t_j)}{\partial x_k} \right)^2 \right) \quad (24)$$

$$\text{Local void fraction}: \alpha_k(t) = \frac{1}{N_e} \sum_{m=1}^{N_e} \left(\frac{1}{N_w} \sum_{j=1}^{N_w} X_k(t+t_j) \right) \quad (25)$$

where X_k is the phase indicator function for phase-k, $u_m'^i(t+t_j) = u_m^i(t+t_j) - U_i(t)$ is the fluctuation of velocity component-i computed during the ensemble run m at the time instant $t+t_j$; N_e is the number of ensemble runs, N_w is the number of velocity samples in each window, t is the current time, $t_j = (j - N_w/2)\Delta t$ is the local window time, and Δt is the time step. An example of fluctuating axial velocity along with gas phase indicator function (X_2) is shown in Fig. 11. Due to the low gas volume fraction in the flow it is clear that

the gas phase statistical data has much smaller sample size than the liquid data. Table 6 summarizes the amount of data we have used to provide the averaged results discussed subsequently in the text.

4.1. Multiple bubble case

Let us now consider the averaged statistics for the multiple bubble flow case. We will not present the single bubble averaged result herein due to the very small volume fraction of the flow and thus, the very small statistical sample of the gas phase from the single bubble simulations.

Fig. 12 shows the lateral distribution of the liquid and gas mean velocities, gas volume fraction and relative velocity of the phases. Note that the equivalent bubble diameter is the same as the distance between vertical gridlines shown in the plot. In order to gather more statistical data for this case we have performed five simulations with different initial perturbations to obtain statistical independence of the simulations.

To obtain this average we have used 5810 time steps ensemble-averaged across 5 runs which resulted in 29,050 time steps of statistical data. This number of time steps corresponds
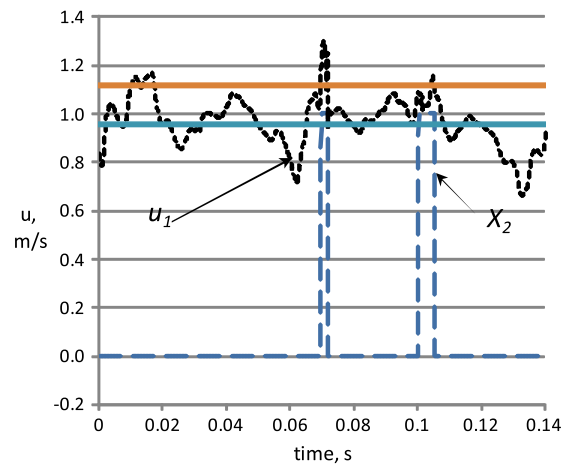

Fig. 11. Example of DNS data produced by PHASTA for two-phase flow at a fixed point which was used for obtaining averaged data (u_1 is the axial velocity component and X_2 is the gas phase indicator function; averaged values U_1^1 and U_1^2 are shown in blue and orange, respectively). (For interpretation of the references to colour in this figure legend, the reader is referred to the web version of this article.)

Table 6
Overview of data used for statistical analysis.

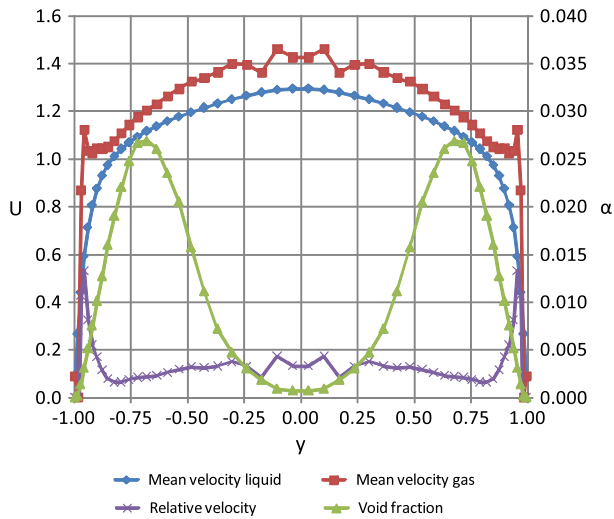| Case:	Single-phase flow	Multiple bubbles	Large bubble
Number of time steps in each run	6081	5810	6668
Number of ensemble runs	1	5	1
Total number of time steps	6081	29,050	6668
Data averaging interval over all ensemble runs, bulk time units	115	88.7	17.45

Fig. 12. Mean flow parameters for multiple bubble simulation (both U and y are non-dimensional).

to approximately one flow through of the liquid phase in each simulation of the ensemble.

We can see that the wall peaked void fraction distribution in Fig. 12 is consistent with the experimental and theoretical observations for small bubbles flowing in conduits (Lahey, 2005), in which the mean velocity gradient induces a lift force on the bubbles which brings them close to the walls. This can also be observed in the simulation snapshots (Fig. 9).

While the mean liquid velocity shows a very smooth profile the gas, while the relative velocity profiles are less perfect (particularly near the center line) due to a smaller sample size. We can observe somewhat singular behavior near the center line, where the local gas volume fraction falls to just 0.07%. This low value results in only capturing the statistics for a few bubbles. As expected, the near wall gas velocity profile is quite uniform compared with the liquid profile since a single bubble occupies a distance of about its diameter near the wall and those bubbles slide along the laminar sublayer, which is captured in the statistics.

The relative velocity (U_R) was observed to be in the range of 0.1–0.17 m/s, excluding the near wall and centerline regions. We note that a simple balance between the drag force and buoyancy force for a sphere in a quiescent liquid results in a 0.26 m/s analytical estimate of the relative velocity. The difference may be attributed to the fact the bubbles are generally not spherical in this case and traveling in the regions with mean liquid velocity gradients. Indeed, Legendre and Magnaudet (1998) have observed that the drag coefficient on a bubble in a linear shear flow is higher than in a non-shear case which would result in a smaller relative velocity.

4.2. Large bubble case

Fig. 13 shows the averaged results for the large bubble turbulent channel flow case. We observe that the large bubbles are not

influenced by the mean liquid velocity gradient in the same way as the small ones. Indeed, in accordance with expectations (Lahey, 2005), the peak in the void fraction distribution is at the center line. In this case we also observe a higher relative velocity (U_R) of 0.227 m/s (when averaged across the channel).

Joseph (2003) proposed a drag coefficient for a spherical cap bubble in the following form:

$$C_D = 0.445\left(6.0 + \frac{32.0}{\mathrm{Re}_{eq}}\right) \tag{26}$$

where $\mathrm{Re}_{eq} = \frac{D_{eq}U_R}{\nu}$ is the Reynolds number of the bubble based on relative velocity and volume equivalent diameter (corresponding to the diameter of a spherical bubble with the same volume as the cap bubble under consideration). In our case $\mathrm{Re}_{eq} = 620.6$ (based on the observed relative velocity) which results in $C_D = 2.69$. Note that the Reynolds number used in Joseph's model has a negligible influence (less than 1%) on the overall result in the observed range of relative velocities. The use of this analytical drag coefficient to estimate the theoretical relative velocity by balancing drag and buoyancy forces results in relative velocity value of 0.206 m/s, which is close to the computed value of 0.227 m/s.

4.3. Liquid phase analysis

In this section we look at the changes in the liquid phase which occur in the presence of bubbles. We compare the mean flow parameters (i.e., mean velocity, turbulent kinetic energy and turbulence dissipation rate) obtained from the multiple bubble and large bubble simulations with the corresponding turbulent single-phase flow. Fig. 14 shows the mean liquid velocity profiles for the three cases of interests. We can observe that the presence of the positively buoyant air bubbles accelerates the liquid up the channel.

The change of the liquid velocity averaged across the channel is linear with respect to the void fraction in the flow for the cases considered (Table 7).

The presence of bubbles in the turbulent flow introduces additional velocity fluctuations into the liquid turbulence. To quantify the amount of this additional kinetic energy we have computed and compared the turbulent kinetic energy of the liquid in the single-phase and two-phase channel flow cases.
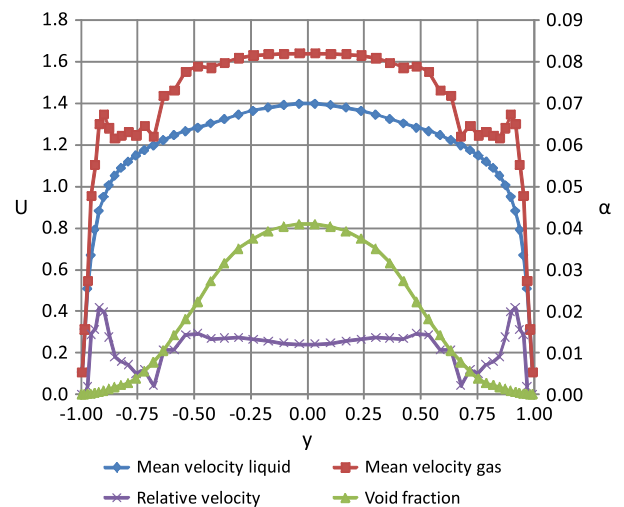

Fig. 13. Mean flow parameters for the large bubble turbulent channel flow case (all dimensional variables show Figs. 11–14 have been non-dimensionalized according to the scaling constants shown in Table 3).
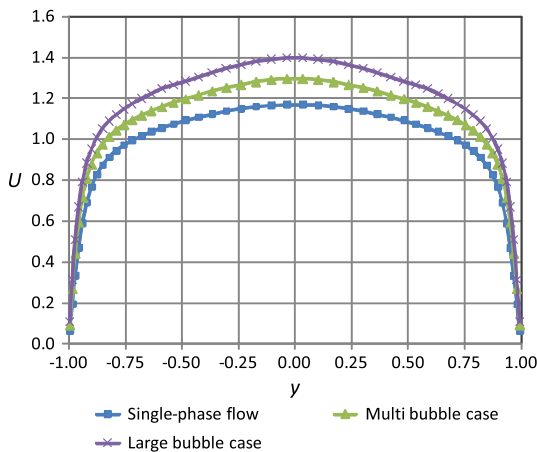
Fig. 14. Mean liquid velocity profiles for single-phase and two-phase flows (both U and y are non-dimensional).

Table 7
Average liquid velocity summary.

Case	Global gas volume fraction, $\langle\alpha\rangle$ (%)	Average liquid velocity, $\langle U\rangle$
Single-phase	0	1.0088
Multiple bubble flow	1	1.1169
Large bubble flow	2	1.2037

Fig. 15 shows the lateral distribution of the turbulent kinetic energy in the three cases of interest. It is interesting to note that multiple bubble flow increases the liquid turbulent kinetic energy everywhere in the channel except the centerline location, where the observed volume fraction is close to zero. However, the amount of kinetic energy increase is not large for this case. In contrast, the large bubble case changes the turbulent kinetic energy very significantly. This can be attributed to the shape and size of the large bubble. In fact, the whole pattern of turbulent fluctuations in the flow changes in the presence of the bubble of this size since the wake behind it occupies a significant portion of the domain. To compare the liquid fluctuation patterns, refer to Fig. 6 showing the single-phase instantaneous velocity distribution, Fig. 9 showing multiple bubble case velocity field and Fig. 10 for the large bubble's liquid velocity field. While the velocity field structure is somewhat similar in Figs. 6 and 9, one can notice a visible difference between the velocity field patterns in Figs. 6 and 10.
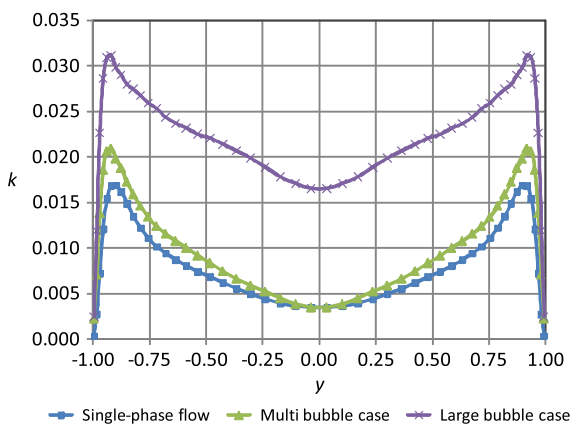
The large changes in velocity magnitude along the channel shown in Fig. 10 result in a significant turbulent kinetic energy difference (Fig. 15). Nevertheless, the lateral shape of the turbulent kinetic energy profiles is similar in all cases under consideration. In addition, these results show that the local bubble-induced turbulence is about an order of magnitude larger for the single cap bubble case than the multiple bubble case, which, in turn, is consistent with the bubble source term commonly used in two-phase k-ε turbulence models (Lahey, 2005), which is $\propto \alpha U_R^3$.

Fig. 16 shows the liquid turbulence dissipation rate distributions. We can observe that values increase across the channel with the increase of void fraction.

The large bubble case exhibits a significant value of the turbulence dissipation rate at the center line compared with the single and multiple bubble flow cases. This can be explained by the presence of high mean shear rates in the wake of the large bubble at the center line while the absence of the small bubble at this location results in very low values of mean shear rate.

4.4. Two-phase Law of the Wall

The multiple bubble and the large bubble liquid velocity profiles were analyzed to evaluate the influence of the presence of the bubbles on the so-called Law of the Wall. The two-phase flow simulations had a different liquid mass flow rate than the original single-phase flow due to the drag force from the bubbles acting on the liquid. Generally, the Law of the Wall should be independent of the Reynolds number. However, for low Reynolds number flows, the constants in the corresponding expression may depend on the Reynolds number. In order to exclude the influence of the mass flow rate change on the Law of the Wall and to provide a better understanding of the bubble's influence on the liquid velocity, the single-phase simulations were re-run using the same liquid flow as in the multiple bubble case and the large bubble case. In this way we have achieved a more natural comparison, consistent with the common interpretation of two-phase flow experiments in which the liquid flow rate (which is practically equal to the total mass flow rate) is kept constant while the gas volume fraction is adjusted by varying the gas volumetric flow rate.

For each void fraction, the appropriate friction velocity was used when converting velocity profiles into wall coordinates. In particular, the friction velocities were obtained using the flow's specific wall shear values:

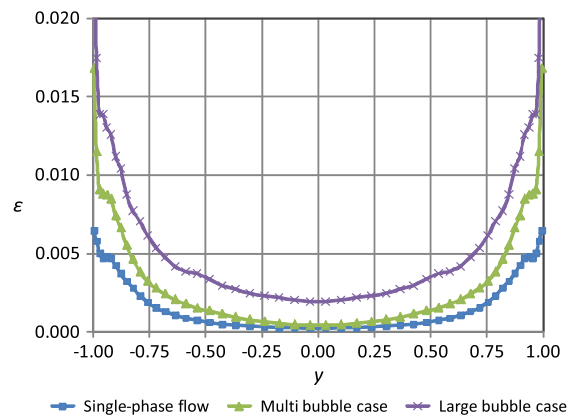$$u_\tau = \sqrt{\frac{\tau_w}{\rho_l}} \tag{27}$$

Fig. 15. Liquid turbulent kinetic energy profiles for single-phase and two-phase flows (both k and y are non-dimensional).

Fig. 16. Liquid turbulent dissipation rate profiles for single-phase and two-phase flows (both ε and y are non-dimensional).

Note that we have used the liquid density in this expression since no bubbles are present at the wall.

There is no universal agreement in the literature on how to estimate the wall shear stress for two-phase bubbly flows. Marie (1987) assumes that since the bubbles do not reach the laminar sublayer, the friction velocity can be found by assuming that the $u^+ = y^+$ law is valid for $y^+ < 5$ in not only the turbulent single-phase flows but also in corresponding two-phase bubbly flows:

$$u_\tau = \sqrt{v_l\left(\frac{dU_L}{dy}\right)_{y=0}} \qquad (28)$$

This assumption results in coincident Law of the Wall plots for both single and two-phase flows in the laminar sublayer.

Another method to estimate the wall shear, τ_w, is to compute it using a fully developed, steady-state force balance (Lahey and Moody, 1993) for each case, where the applied pressure gradient and gravitational force in each simulation is counteracted by the wall shear:

$$V(\nabla p - \rho_m g) = \tau_w A_w \qquad (29)$$

Since the applied pressure gradient and the gravitational force were the input parameters to our simulations, the wall shear was easily determined (see Table 8). However, this approach may result in significant errors, since typically both the total pressure gradient and gravity force are large compared to their difference (see Table 5). In particular, in the multiple bubble turbulent flow simulations the difference between those quantities was about 5% of the pressure gradient value. If we assume only a 0.1% margin of error for the pressure gradient and gravity force, it would result in approximately 2% error in the computed wall shear stress value.

Nevertheless, we have used both methods to estimate the two-phase Law of the Wall observed in the current DDNS results. That is, both the laminar sublayer method and the force balance method were used. Table 8 summarizes the parameters of the two supplemental single-phase cases along with corresponding two-phase flows using these two methods for estimating the wall shear stress.

Figs. 17 and 18 compare the multiple bubble case with the same liquid mass flow rate single phase case. We can see that for both single and two-phase DDNS a constant slope region (i.e., the Law of the Wall) is present:

$$u^+ = \frac{1}{\kappa_0} \ln y^+ + C \qquad (30)$$

However, the parameters κ_0 and C are different for the two-phase simulation. We note that laminar sublayer region in Fig. 17 overlaps for the single and two-phase flow simulations, as expected for this case.

We can see that in both cases the multiple bubble flow simulations the slope of the Law of the Wall velocity profile is less steep that in the corresponding single-phase flow. Figs. 19 and 20 present a similar trend by comparing the large bubble case liquid velocity profile to a single-phase flow. However, for a single large bubble the change in slope is significantly more pronounced.
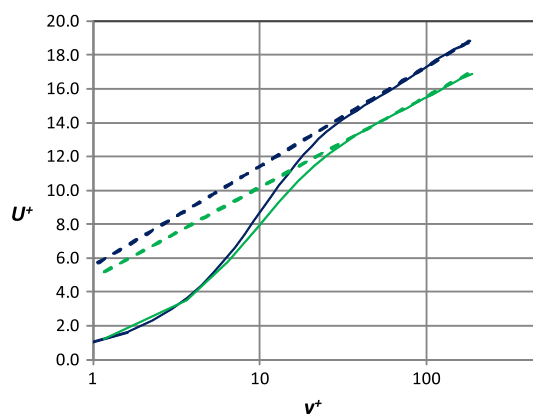

Fig. 17. Velocity profiles (solid lines) compared to the appropriate Law of the Wall (dashed lines). Single-phase (blue) and 1% bubbly flow (green) are shown based on the laminar sublayer assumption. (For interpretation of the references to colour in this figure legend, the reader is referred to the web version of this article.)
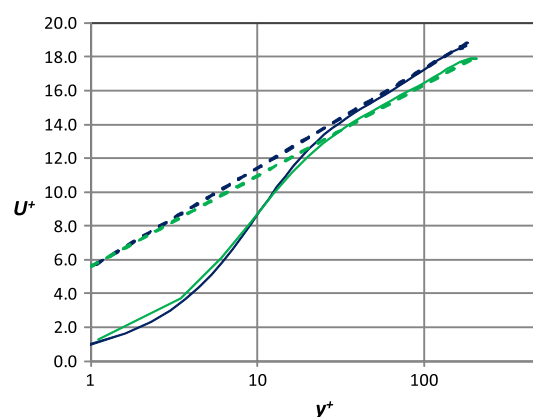

Fig. 18. Velocity profiles (solid lines) compared to the appropriate Law of the Wall (dashed lines). Single-phase (blue) and 1% bubbly flow (green) are shown based on a force balance. (For interpretation of the references to colour in this figure legend, the reader is referred to the web version of this article.)

We have evaluated these slopes (dashed lines in Figs. 17–20) and summarized the results in Table 9. Note that the all single-phase cases follow the Law of the Wall with the same coefficients.

It is interesting to note that the trends observed in the present virtual experiments (i.e., a decreasing slope of the logarithmic velocity profile, or increasing κ_0, with increasing void fraction) are similar to the experimental data reported by Marie et al. (1997), although their experiments were performed for a different geometry (a vertical plate submerged in a large rectangular channel and for dispersed bubbly flows having a range of void fractions up to 1.5%). Nevertheless, as it can be seen, the standard logarithmic Law of the Wall curve is very sensitive to the wall shear.

In the present case the wall shear could only be estimated from the averaged PHASTA results, thus to further demonstrate the effect of void fraction on liquid velocity in a more direct manner, non-dimensional liquid velocity profiles, using the average liquid

Table 8
Liquid mass flow rates and wall shear stresses.

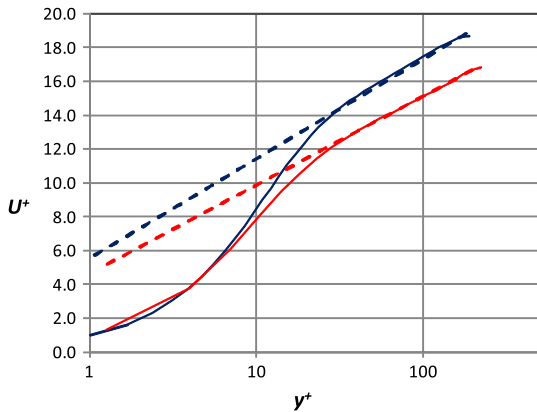| Case	Void fraction, $\langle\alpha\rangle$ (%)	Liquid superficial velocity, $\langle U \rangle$	Wall shear stress based on the laminar sublayer assumption (N/m²)	Wall shear stress based on a force balance (N/m²)
Single-phase flow (case-1)	0	1.1051	0.00477	0.00480
Multiple bubble flow	1	1.1050	0.005853	0.005242
Single-phase flow (case-2)	0	1.1757	0.005072	0.005252
Large bubble flow	2	1.1756	0.006929	0.008729

Fig. 19. Velocity profiles (solid lines) compared to the appropriate Law of the Wall (dashed lines). Single-phase (blue) and 2% large bubble flow (red) are shown based on laminar sublayer assumption. (For interpretation of the references to colour in this figure legend, the reader is referred to the web version of this article.)
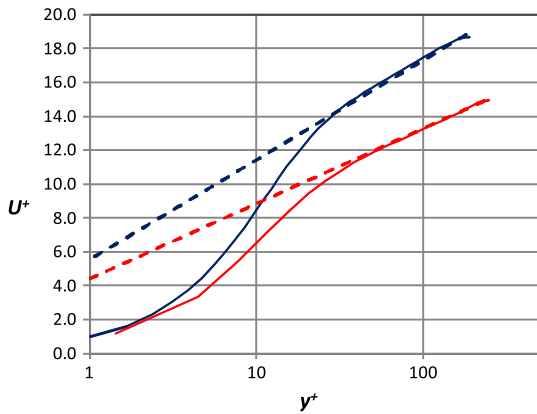

Fig. 20. Velocity profiles (solid lines) compared to the appropriate Law of the Wall (dashed lines). Single-phase (blue) and 2% large bubble flow (red) are shown based on a force balance. (For interpretation of the references to colour in this figure legend, the reader is referred to the web version of this article.)

Table 9
Law of the Wall parameters.

Case	Void fraction (%)	κ_0	C
Single-phase	0	0.39	5.5
Multiple bubble flow, laminar sublayer method	1	0.43	5.6
Multiple bubble flow, force balance method	1	0.43	4.8
Large bubble flow, laminar sublayer method	2	0.52	4.4
Large bubble flow, force balance method	2	0.44	4.6

velocities ($\langle U \rangle$, in Table 7) and half channel width (δ) as the parameters of reference, are shown in Fig. 21. In those coordinates the velocity profiles are essentially the same in the logarithmic zone of the Law of the Wall, however, in the viscous sublayer we see, as expected, an increase of the liquid velocity in the two-phase flow simulations. Note that the results shown in Fig. 21 are free of the inaccuracies associated with indirectly estimating the wall shear.

5. Conclusions

The detached direct numerical simulation (DDNS) results presented in this paper demonstrate that the complex interactions between gas bubbles and the turbulent liquid flows can be
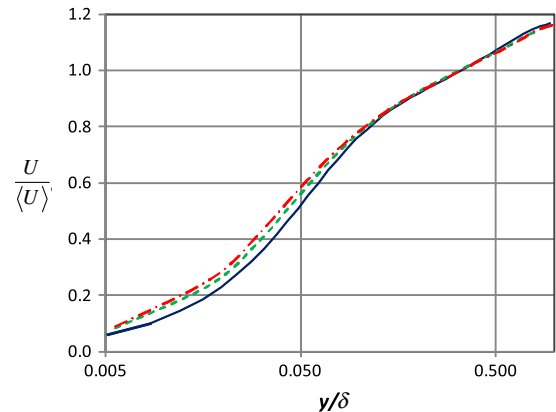

Fig. 21. Liquid velocity profiles obtained from single-phase (solid line), multiple bubble (dashed line) and large bubble (dash-dot line) simulations scaled using the mean liquid velocity ($\langle U \rangle$) and channel half-width (δ).

numerically resolved and analyzed. The detailed two-phase DDNS data provided by the present study help us better understand turbulent bubbly flows and they can be used in the development of advanced models of turbulence in two-phase bubbly flows, similar to those done previously for single-phase (Bolotnov et al., 2009) and some two-phase turbulent flows (Bolotnov et al., 2008a,b).

Two different types of bubbly flows were simulated and analyzed. The shape of the volume fraction distribution for those flows was consistent with experimental observations. Interestingly the influence of a large bubble on the surrounding was relatively strong compared to a dispersed bubbly flow, both in the Law of the Wall plots and in the turbulent kinetic energy profiles. Nevertheless, additional simulations at a fixed volume fraction for different bubble sizes would provide more information regarding the influence of bubble size on the liquid's turbulence behavior.

It has been demonstrated that DNS simulations of two-phase flows can be performed for Reynolds numbers corresponding to fully-developed turbulent flows. Also, it has been shown the results of such simulations yield consistent information about several time-averaged flow characteristics, such as local distributions of velocity, turbulent kinetic energy and turbulent energy dissipation. Furthermore, the proposed approach allows one to formulate a two-phase version of the "Law of the Wall" for gas/liquid flows with bubbles of different size, from small nearly spherical to large characterized by a high degree of instantaneous deformation.

Future simulations should also include higher void fraction flows as well as different conduit flow regimes (e.g., slug flow, churn-turbulent and annular flow). High void fraction flows are particularly interesting, since such flows are common to a wide range of practical problems and the existing experimental techniques do not allow one to acquire detailed and reliable data.

Finally, to better validate the DDNS approach presented herein, future experiments should focus on direct measurements of wall shear in turbulent multiphase channel flows at low Reynolds numbers, but over a wider range of void fractions (up to 10–20%).

Acknowledgements

References

Bolotnov, I.A., Lahey Jr., R.T., Drew, D.A., Jansen, K.E., 2008a. Turbulent cascade modeling of single and bubbly two-phase turbulent flows. Int. J. Multiphase Flow 34, 1142–1151.

Bolotnov, I.A., Lahey Jr., R.T., Drew, D.A., Jansen, K.E., Oberai, A.A., 2008b. A spectral turbulent cascade model for single and two-phase uniform shear flows. J. Turbul. 9, 1–18.

Bolotnov, I.A., Lahey Jr., R.T., Drew, D.A., Jansen, K.E., Oberai, A.A., 2009. Spectral cascade modeling of turbulent flow in a channel. Jpn. J. Multiphase Flow 23, 190–204.

Brackbill, J.U., Kothe, D.B., Zemach, C., 1992. A continuum method for modeling surface tension. J. Comput. Phys. 100, 335–354.

Bunner, B., Tryggvason, G., 2003. Effect of bubble deformation on the properties of bubbly flows. J. Fluid Mech. 495, 77–118.

Clift, R., Grace, J.R., Weber, M.E., 1978. Bubbles, Drops and Particles. Academic Press.

Joseph, D.D., 2003. Rise velocity of a spherical cap bubble. J. Fluid Mech. 488, 213–223.

Lahey, R.T., Jr., Moody, F.J., 1993. The Thermal-Hydraulics of a Boiling Water Nuclear Reactor. ANS Monograph, second ed., pp. 239–240.

Lahey Jr., R.T., 2005. The simulation of multidimensional multiphase flows. Nucl. Eng. Des. 235, 1043–1060.

Lance, M., Marie, J.L., Moursali, E., Bataille, J., Suzanne, C., Roig, V., Bel Fdhila, R., Masbernat, L., 1996. Experimental study of turbulent bubbly shear flows. Chem. Eng. Commun., 51–70.

Legendre, D., Magnaudet, J., 1998. The lift force on a spherical bubble in a viscous linear shear flow. J. Fluid Mech. 368, 81–126.

Lu, J., Tryggvason, G., 2008. Effect of bubble deformability in turbulent bubbly upflow in a vertical channel. Phys. Fluids 20, 040701.

Marie, J.L., 1987. Modelling of the skin friction and heat transfer in turbulent two-component bubbly flows in pipes. Int. J. Multiphase Flow 13, 309–325.

Marie, J.L., Moursali, E., Tran-Cong, S., 1997. Similarity law and turbulence intensity profiles in a bubbly boundary layer at low void fractions. Int. J. Multiphase Flow 23, 227–247.

Moser, R., Kim, J., Mansour, N., 1999. Direct numerical simulation of turbulent channel flow up to $Re_\tau = 590$. Phys. Fluids 11, 943–945.

Nagrath, S., 2004. Adaptive Stabilized Finite Element Analysis of Multi-Phase Flows Using a Level Set Approach, Ph.D. Thesis, MANE. Rensselaer Polytechnic Institute, 130 p.

Nagrath, S., Jansen, K.E., Lahey Jr., R.T., 2005. Computation of incompressible bubble dynamics with a stabilized finite element level set method. Comput. Methods Appl. Mech. Eng. 194, 4565–4587.

Nicoud, F., Winckelmans, G., Carati, D., Baggett, J., Cabot, W., 1998. Boundary conditions for LES away from the wall, Center for Turbulence Research. In: Proceedings of the Summer Program 1998, Stanford University, pp. 413–422.

Nierhaus, T., Abeele, D.V., Deconinck, H., 2007. Direct numerical simulation of bubbly flow in the turbulent boundary layer of a horizontal parallel plate electrochemical reactor. Int. J. Heat Fluid Flow 28, 542–551.

Orszag, S., 1971. Accurate solution of Orr-Sommerfeld stability equation. J. Fluid Mech. 50, 689–703.

Pang, M., Wei, J., Yu, B., Kawaguchi, Y., 2010. Numerical investigation on turbulence and bubbles distribution in bubbly flow under normal gravity and microgravity conditions. Microgravity Sci. Technol. 22, 283–294.

Serizawa, A., Kataoka, L., Michiyoshi, I., 1975a. Turbulence structure of air/water bubbly flow. II. Local properties. Int. J. Multiphase Flow 2, 235–246.

Serizawa, A., Kataoka, L., Michiyoshi, I., 1975b. Turbulence structure of air/water bubbly flow. III. Transport properties. Int. J. Multiphase Flow 2, 247–259.

Sethian, J.A., 1999. Level Set Methods and Fast Marching Methods. Cambridge University Press.

Spalding, D.B., 1961. A single formula for the law of the wall. ASME J. Appl. Math. 28, 455–458.

Sussman, M., Fatemi, E., 1999. An efficient, interface-preserving level set re-distancing algorithm and its application to interfacial incompressible fluid flow. Siam J. Sci. Comput. 20, 1165–1191.

Sussman, M., Fatemi, E., Smereka, P., Osher, S., 1998. An improved level set method for incompressible two-phase flows. J. Comput. Fluids 27, 663–680.

Sussman, M., Almgren, A.S., Bell, J.B., Colella, P., Howell, L.H., Welcome, M.L., 1999. An adaptive level set approach for incompressible two-phase flows. J. Comput. Phys. 148, 81–124.

Toutant, A., Labourasse, E., Lebaigue, O., Simonin, O., 2008. DNS of the interaction between a deformable buoyant bubble and a spatially decaying turbulence: a priori tests for LES two-phase flow modelling. Comput. Fluids 37, 877–886.

Trofimova, A., Tejada-Martinez, A.E., Jansen, K.E., Lahey Jr., R.T., 2009. Direct numerical simulation of turbulent channel flows using a stabilized finite element method. Comput. Fluids 38, 924–938.

Tryggvason, G., Esmaeeli, A., Lu, J., Biswas, S., 2006. Direct numerical simulations of gas/liquid multiphase flows. Fluid Dyn. Res. 38, 660–681.

Wang, S.K., Lee, S.J., Jones, O.C.J., Lahey Jr., R.T., 1987. 3-D turbulence structure and phase distribution measurements in bubbly two-phase flows. Int. J. Multiphase Flow 13, 327–343.

Whiting, C.H., 1999. Stabilized Finite Element Methods for Fluid Dynamics Using a Hierarchical Basis, Ph.D. Thesis, MEAE, Rensselaer Polytechnic Institute, Troy, NY.